Analysis of the Spatial Distribution of Galaxies by Multiscale Methods

J-L. Starck
DAPNIA/SEDI-SAP, Service d'Astrophysique,
CEA-Saclay, 91191 Gif-sur-Yvette, France

V.J. Martínez
Observatori Astronòmic de la Universitat de
València, Edifici d'Instituts de Paterna, Apartat de Correus
22085, 46071 València, Spain

D. L. Donoho, O. Levi
Department of Statistics, Stanford University,
Sequoia Hall, Stanford, CA 94305, USA

P. Querre
DAPNIA/SEDI-SAP, Service d'Astrophysique,
CEA-Saclay, 91191 Gif-sur-Yvette, France

E. Saar
Tartu Observatory, Toravere, 61602 Estonia

February 23, 2005

Abstract

Galaxies are arranged in interconnected walls and filaments forming a cosmic web encompassing huge, nearly empty, regions between the structures. Many statistical methods have been proposed in the past in order to describe the galaxy distribution and discriminate the different cosmological models. We present in this paper multiscale geometric transforms sensitive to clusters, sheets and walls: the 3D isotropic undecimated wavelet transform, the 3D ridgelet transform and the 3D beamlet transform. We show that statistical properties of transform coefficients measure in a coherent and statistically reliable way, the degree of clustering, filamentarity, sheetedness, and voidedness of a dataset.

Keywords

Galaxy distribution, large scale structures, wavelet, ridgelet, beamlet, multi-scale methods.

1 Introduction

Galaxies are not uniformly distributed throughout the universe. Voids, filaments, clusters, and walls of galaxies can be observed, and their distribution constrains our cosmological theories.

Therefore we need reliable statistical methods to compare the observed galaxy distribution with theoretical models and cosmological simulations.

The standard approach for testing models is to define a point process which can be characterized by statistical descriptors. This could be the distribution of galaxies of a specific type in deep redshift surveys of galaxies (or of clusters of galaxies) [1]. In order to compare models of structure formation, the different distribution of dark matter particles in N-body simulations could be analyzed as well, with the same statistics.

The two-point correlation function $\xi(r)$ has been the primary tool for quantifying large-scale cosmic structure [22]. Assuming that the galaxy distribution in the Universe is a realization of a stationary and isotropic random process, the two-point correlation function can be defined from the probability δP of finding an object within a volume element δV at distance r from a randomly chosen object or position inside the volume: $\delta P = n(1 + \xi(r))\delta V$, where n is the mean density of objects. The function $\xi(r)$ measures the clustering properties of objects in a given volume. It is zero for a uniform random distribution, positive (respectively, negative) for a more (respectively, less) clustered distribution. For a hierarchical clustering or fractal process, $1 + \xi(r)$ follows a power-law behavior with exponent $D_2 - 3$. Since $\xi(r) \sim r^{-\gamma}$ for the observed galaxy distribution, the correlation dimension for the range where $\xi(r) \gg 1$ is $D_2 \simeq 3 - \gamma$. The Fourier transform of the correlation function is the power spectrum. The direct measurement of the power spectrum from redshift surveys is of major interest because model predictions are made in terms of the power spectral density. It seems clear that the real space power spectrum departs from a single power-law ruling out simple unbounded fractal models [30]. The two-point correlation function can been generalized to the N-point correlation function [29, 23], and all the hierarchy can be related with the physics responsible for the clustering of matter. Nevertheless they are difficult to measure, and therefore other related statistical measures have been introduced as a complement in the statistical description of the spatial distribution of galaxies [18], such as the void probability function [19], the multifractal approach [16], the minimal spanning tree [1, 13, 8], the Minkowski functionals [20, 11] or the J function [15, 12] which is defined as the ratio $J(r) = \frac{1-G(r)}{1-F(r)}$, where F is the distribution function of the distance r of an arbitrary point in $\mathbf{R}^3$ to the nearest object in the catalog, and G is the distribution function of the distance r of an object to the nearest object. Wavelets have also been used for analyzing the projected 2D or the 3D galaxy distribution [9, 24, 17, 21, 14].

New geometric multiscale methods have recently emerged, the beamlet transform [4, 6] and the ridgelet transform [3]; these allow us to represent data containing respectively filaments and sheets, while wavelets represent well isotropic features (i.e. clusters in 3D). As each of these three transforms is tuned to on specific kind of feature, all of them are useful and should be combined to describe a given catalog.

Sections 2, 3 and 4 describe respectively the 3D wavelet transform, the 3D ridgelet transform and the 3D beamlet transform. It is shown in section 5 through a set of of experiments how these three 3D transforms can be combined in order to describe statistically the distribution of galaxies.

[1] Making 3D maps of galaxies requires knowing how far away each galaxy is from Earth. One way to get this distance is to use Hubble's law for the expansion of the universe and to measure the shift, called redshift, to redder colors of spectral features in the galaxy spectrum. The greater the redshift, the larger the velocity, and, by Hubble's law, the larger the distance.

2 The 3D Wavelet Transform

2.1 The Undecimated Isotropic Wavelet Transform

For each $a > 0$, $b_1, b_2, b_3 \in \mathbf{R}^3$, the *wavelet* is defined by

$$\psi_{a,b_1,b_2,b_3} : \mathbf{R}^3 \to \mathbf{R}$$
$$\psi_{a,b_1,b_2,b_3}(x_1, x_2, x_3) = a^{-3/2} \cdot \psi(\tfrac{x_1-b_1}{a}, \tfrac{x_2-b_2}{a}, \tfrac{x_3-b_3}{a})$$

Given a function $f \in L^2(\mathbf{R}^3)$, we define its wavelet coefficients by:

$$\mathcal{W}_f : \mathbf{R}^4 \to \mathbf{R}$$
$$\mathcal{W}_f(a, b_1, b_2, b_3) = \int \overline{\psi}_{a,b_1,b_2,b_3}(\mathbf{x}) f(\mathbf{x}) d\mathbf{x}.$$

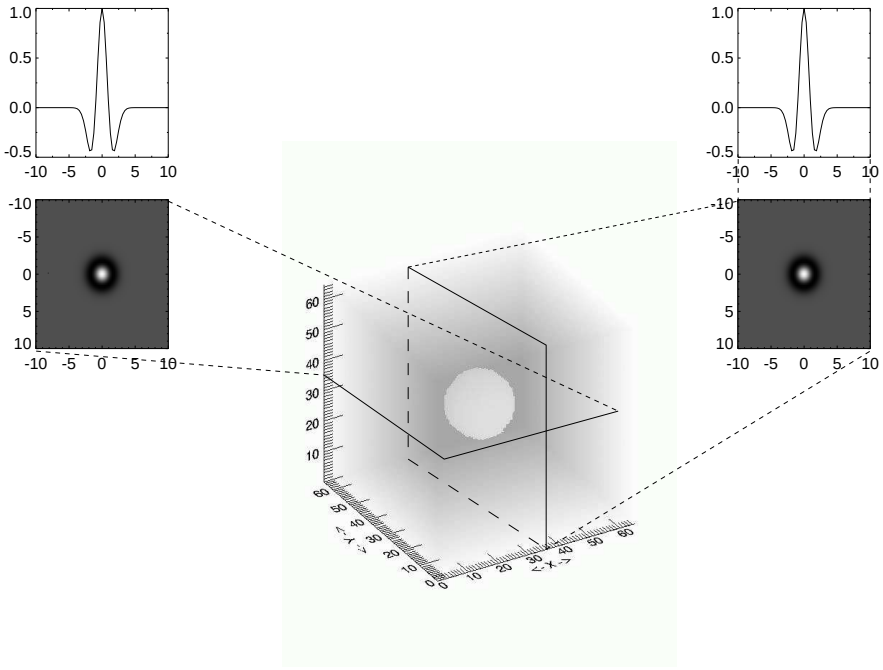

Figure 1: Example of wavelet function.

Figure 1 shows an example of 3D wavelet function.

It is standard to digitize the transform for data $c(x, y, z)$ with $x, y, z \in \{1, \ldots, N\}$ as follows. The wavelet transform of a signal produces, at each scale j, a set of zero-mean coefficient values $\{w_j\}$. Let ϕ be a lowpass filter and let define $\phi_j(x) = \phi(2^j x)$ and $c_j = c * \phi_j$. Using an undecimated isotropic wavelet decomposition [28], the set $\{w_j\}$ has the same number of pixels as the signal and this wavelet transform is redundant. Furthermore, using a wavelet defined as the difference between the scaling functions of two successive scales

$$\frac{1}{8}\psi(\frac{x}{2}, \frac{y}{2}, \frac{z}{2}) = \phi(x, y, z) - \frac{1}{8}\phi(\frac{x}{2}, \frac{y}{2}, \frac{z}{2}), \tag{1}$$

the original cube $c = c_0$ can be expressed as the sum of all the wavelet scales and the smoothed array c_J

$$c_{0,x,y,z} = c_{J,x,y,z} + \sum_{j=1}^{J} w_{j,x,y,z}. \tag{2}$$

The set $w = \{w_1, w_2, ..., w_J, c_J\}$ represents the wavelet transform of the data. If we let $\mathcal{W}$ denote the wavelet transform operator and N the pixels in c, the wavelet transform w ($w = \mathcal{W}c$) has

$(J+1)N$ pixels, for a redundancy factor of $J+1$. The scaling function ϕ is generally chosen as a spline of degree 3, and the 3D implementation is based on three 1D sets of (separable) convolutions. Like the scaling function ϕ, the wavelet function ψ is isotropic. More details can be found in [28, 27].

3 The 3D Ridgelet Transform

3.1 The 2D Ridgelet Transform

The two-dimensional continuous ridgelet transform of a function $f \in L^2(\mathbf{R}^2)$ was defined in [3] as follows.
Select a smooth function $\psi \in L^2(\mathbf{R})$, satisfying *admissibility* condition

$$\int |\hat{\psi}(\xi)|^2/|\xi|\, d\xi < \infty, \tag{3}$$

which holds if ψ has a sufficient decay and a vanishing mean $\int \psi(t)dt = 0$ (ψ can be normalized so that it has unit energy $1/(2\pi)\int |\hat{\psi}(\xi)|^2 d\xi = 1$). For each $a > 0$, $b \in \mathbf{R}$ and $\theta_1 \in [0, 2\pi[$, we define the *ridgelet* by

$$\begin{aligned} \psi_{a,b,\theta_1} : \quad & \mathbf{R}^2 \to \mathbf{R} \\ & \psi_{a,b,\theta_1}(x_1, x_2) = a^{-1/2} \cdot \psi((x_1 \cos\theta_1 + x_2 \sin\theta_1 - b)/a); \end{aligned}$$

Given a function $f \in L^2(\mathbf{R}^2)$, we define its ridgelet coefficients by:

$$\begin{aligned} \mathcal{R}_f : \quad & \mathbf{R}^3 \to \mathbf{R} \\ & \mathcal{R}_f(a, b, \theta_1) = \int \overline{\psi}_{a,b,\theta_1}(\mathbf{x}) f(\mathbf{x}) d\mathbf{x}. \end{aligned}$$

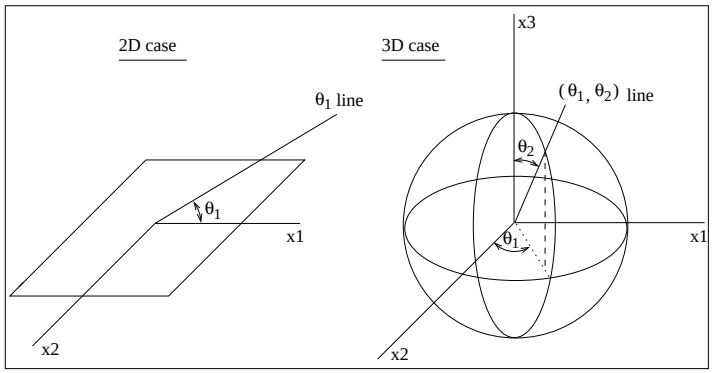

Figure 2: Definition of angle1 θ_1 and θ_2 in $\mathbf{R}^2$ and $\mathbf{R}^3$

It has been shown [3] that the ridgelet transform is precisely the application of a 1-dimensional wavelet transform to the slices of the Radon transform (where the angular variable θ_1 is constant). This method is in a sense optimal to detect lines of the size of the image (the integration increase as the length of the line). More details on the implementation of the digital ridgelet transform can be found in [26].

Figure 3 (left) shows an example ridgelet function. This function is constant along lines $x_1 \cos\theta + x_2 \sin\theta = const$. Transverse to these ridges it is a wavelet (see figure 3 (right).

3.2 From 2D to 3D

The three-dimensional continuous ridgelet transform of a function $f \in L^2(\mathbf{R}^3)$ is given by:

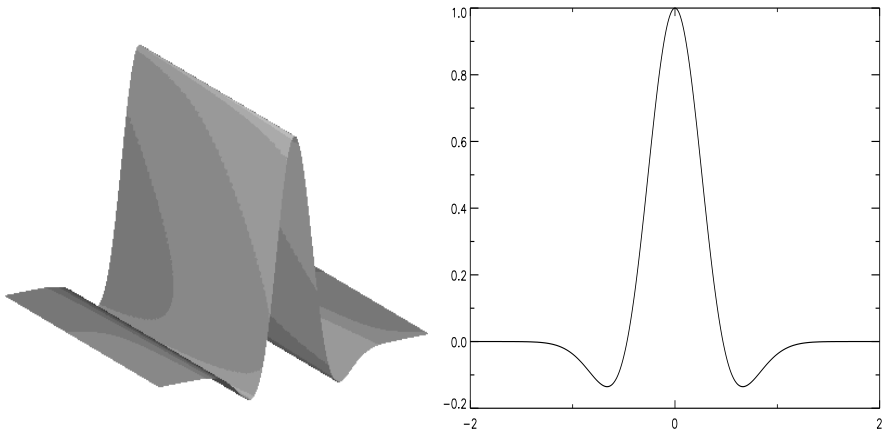

Figure 3: Example of 2D ridgelet function.

$$\mathcal{R}_f : \quad \mathbf{R}^4 \to \mathbf{R}$$
$$\mathcal{R}_f(a,b,\theta_1,\theta_2) = \int \overline{\psi}_{a,b,\theta_1,\theta_2}(\mathbf{x}) f(\mathbf{x}) d\mathbf{x}.$$

where $a > 0$, $b \in \mathbf{R}$, $\theta_1 \in [0, 2\pi[$ and $\theta_2 \in [0, \pi[$.
The *ridgelet* function is defined by:

$$\psi_{a,b,\theta_1,\theta_2} : \quad \mathbf{R}^3 \to \mathbf{R}$$
$$\psi_{a,b,\theta_1,\theta_2}(x_1,x_2,x_3) = a^{-1/2} \cdot \psi((x_1 \cos\theta_1 \cos\theta_2 + x_2 \sin\theta_1 \cos\theta_2 + x_3 \sin\theta_2 - b)/a);$$

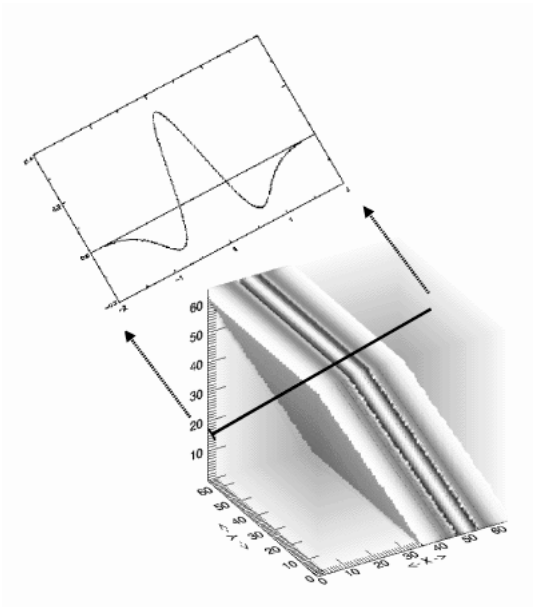

Figure 4: Example of ridgelet function.

Figure 4 shows an example of ridgelet function. It is a wavelet function in the direction defined by the line (θ_1, θ_2), and it is constant along the orthogonal plane to this line.

As in the 2D case, the 3D ridgelet transform can be built by extracting lines in the Fourier domain. Let $c(i_1, i_2, i_3)$ be a cube of size (N, N, N); the algorithm consists in the following steps:

1. *3D-FFT.* Compute $\hat{c}(k_1, k_2, k_3)$, the three-dimensional FFT of the cube $c(i_1, i_2, i_3)$.

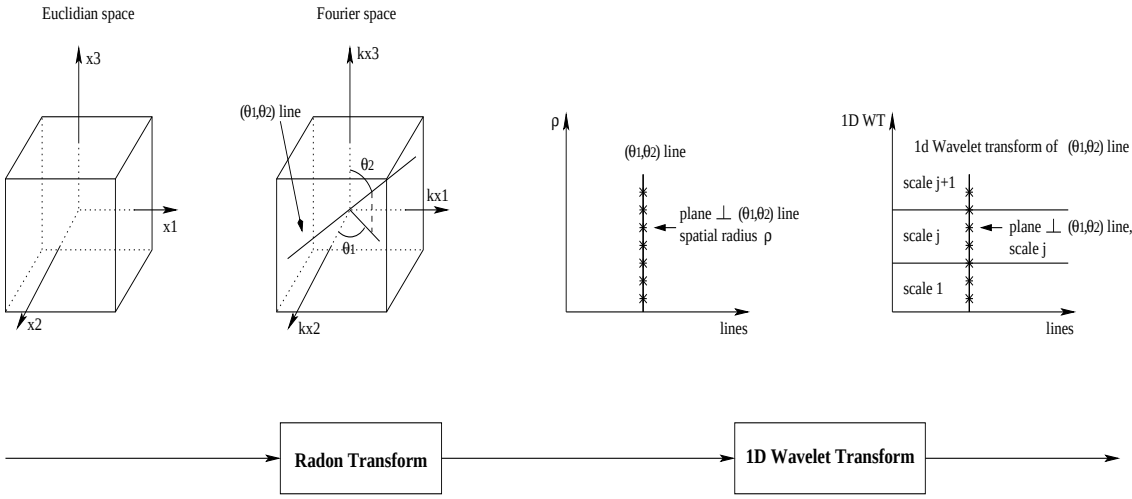

Figure 5: 3D ridgelet transform flowgraph.

2. *Cartesian-to-Spherical Conversion.* Using an interpolation scheme, substitute the sampled values of $\hat{c}$ obtained on the Cartesian coordinate system (k_1, k_2, k_3) with sampled values in a spherical coordinate system $(\theta_1, \theta_2, \rho)$.

3. *Extract lines.* Extract the $3N^2$ lines (of size N) passing through the origin and the boundary of $\hat{c}$.

4. *1D-IFFT.* Compute the one-dimensional inverse FFT on each line.

5. *1D-WT.* Compute the one-dimensional wavelet transform on each line.

Figure 5 the 3D ridgelet transform flowgraph. The 3D ridgelet transform allows us to detect sheets in a cube.

Local 3D Ridgelet Transform

The ridgelet transform is optimal to find sheets of the size of the cube. To detect smaller sheets, a partitioning must be introduced [2]. The cube c is decomposed into blocks of lower side-length b so that for a $N \times N \times N$ cube, we count N/b blocks in each direction. After the block partitioning, the tranform is tuned for sheets of size $b \times b$ and of thickness a_j, a_j corresponding to the different dyadic scales used in the transformation.

4 The 3D Beamlet Transform

4.1 Definition

The X-ray transform of a continuum function $f(x, y, z)$ with $(x, y, z) \in \mathbf{R}^3$ is defined by

$$(Xf)(L) = \int_L f(p)dp \tag{4}$$

where L is a line in $\mathbf{R}^3$, and p is a variable indexing points in the line. The transformation contains all line integrals of f. The Beamlet Transform (BT) can be seen as a multiscale digital X-ray transform. It is multiscale transform because, in addition to the multiorientation and multilocation line integral calculation, it integrated also over line segments at different length. The 3D BT is an extension to the 2D BT, proposed by Donoho and Huo [4].

The system of 3D beams

The transform requires an expressive set of line segments, including line segments with various lengths, locations and orientations lying inside a 3D volume.

A seemingly natural candidate for the set of line segments is the family of *all* line segments between each voxel corner and every other voxel corner, the set of *3D beams*. For a 3D data set with n^3 voxels, there are $O(n^6)$ 3D beams. It is infeasible to use the collection of 3D beams as a basic data structure since any algorithm based on this set will have a complexity with lower bound of n^6 and hence be unworkable for typical 3D data size.

4.2 The Beamlet System

A dyadic cube $C(k_1, k_2, k_3, j) \subset [0,1]^3$ is the collection of 3D points

$$\{(x_1, x_2, x_3) : [k_1/2^j, (k_1+1)/2^j] \times [k_2/2^j, (k_2+1)/2^j] \times [k_3/2^j, (k_3+1)/2^j]\}$$

where $0 \le k_1, k_2, k_3 < 2^j$ for an integer $j \ge 0$, called the scale.

Such cubes can be viewed as descended from the unit cube $C(0,0,0,0) = [0,1]^3$ by recursive partitioning. Hence, the result of splitting $C(0,0,0,0)$ in half along each axis is the eight cubes $C(k_1, k_2, k_3, 1)$ where $k_i \in \{0,1\}$, splitting those in half along each axis we get the 64 subcubes $C(k_1, k_2, k_3, 2)$ where $k_i \in \{0,1,2,3\}$, and if we decompose the unit cube into n^3 voxels using a uniform n-by-n-by-n grid with $n = 2^J$ dyadic, then the individual voxels are the n^3 cells $C(k_1, k_2, k_3, J)$, $0 \le k_1, k_2, k_3 < n$.

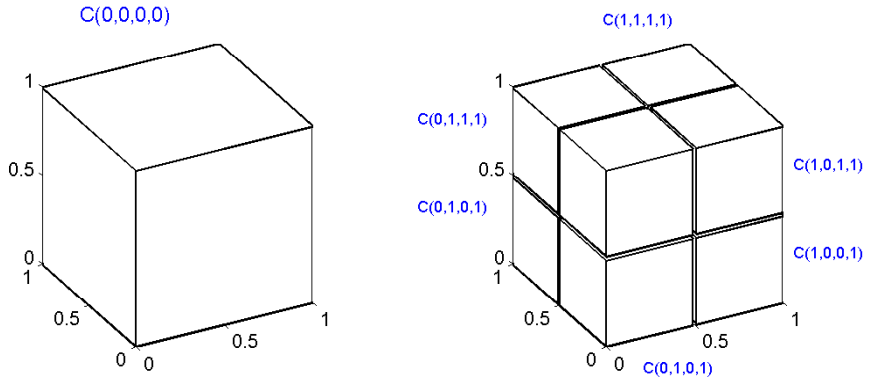

Figure 6: Dyadic cubes

Associated to each dyadic cube we can build a system of line segments that have both of their end-points lying on the cube boundary. We call each such segment *a beamlet*. If we consider all pairs of boundary voxel corners, we get $O(n^4)$ beamlets for a dyadic cube with a side length of n voxels (we actually work with a slightly different system in which each line is parametrized by a slope and an intercept instead of its end-points as explained below). However, we will still have $O(n^4)$ cardinality. Assuming a voxel size of $1/n$ we get $J+1$ scales of dyadic cubes where $n = 2^J$, for any scale $0 \le j \le J$ there are 2^{3j} dyadic cubes of scale j and since each dyadic cube at scale j has a side length of 2^{J-j} voxels we get $O(2^{4(J-j)})$ beamlets associated with the dyadic cube and a total of $O(2^{4J-j}) = O(n^4/2^j)$ beamlets at scale j. If we sum the number of beamlets at all scales we get $O(n^4)$ beamlets.

This gives a multi-scale arrangement of line segments in 3D with controlled cardinality of $O(n^4)$, the scale of a beamlet is defined as the scale of the dyadic cube it belongs to so lower scales correspond to longer line segments and finer scales correspond to shorter line segments. Figure 7 shows 2 beamlets at different scales.

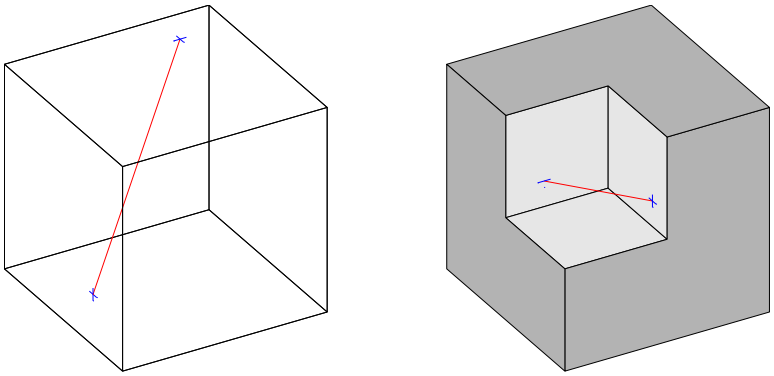

Figure 7: Examples of Beamlets at two different scales. (a) Scale 0 (coarsest scale) (b) Scale 1 (next finer scale).

To index the beamlets in a given dyadic cube we use slope-intercept coordinates. For a data cube of $n \times n \times n$ voxels consider a coordinate system with the cube center of mass at the origin and a unit length for a voxel. Hence, for (x, y, z) in the data cube we have $|x|, |y|, |z| \leq n/2$. We can consider three kinds of lines: *x-driven, y-driven, and z-driven*, depending on which axis provides the shallowest slopes. An x-driven line takes the form

$$z = s_z x + t_z, \quad y = s_y x + t_y$$

with slopes s_z,s_y, and intercepts t_z and t_y. Here the slopes $|s_z|, |s_y| \leq 1$. y- and z-driven lines are defined with an interchange of roles between x and y or z, as the case may be. The slopes and intercepts run through equispaced sets:

$$s_x, s_y, s_z \in \{2\ell/n : \ell = -n/2, \ldots, n/2 - 1\}, \qquad t_x, t_y, t_z \in \{\ell : -n/2, \ldots, n/2 - 1\}.$$

Beamlets in a data cube of side n have lengths between $n/2$ and $\sqrt{3}n$ (the main diagonal).

Computational aspects

Beamlet *coefficients* are line integrals over the set of beamlets. A digital 3D image can be regarded as a 3D piece-wise constant function and each line integral is just a weighted sum of the voxel intensities along the corresponding line segment. Donoho and Levi [6] discuss in detail different approaches for computing line integrals in a 3D digital image. Computing the beamlet coefficients for real application data sets can be a challenging computational task since for a data cube with $n \times n \times n$ voxels we have to compute $O(n^4)$ coefficients. By developing efficient cache aware algorithms we are able to handle 3D data sets of size up to $n = 256$ on a typical desktop computer in less than a day running time. We will mention that in many cases there is no interest in the coarsest scales coefficient that consumes most of the computation time and in that case the over all running time can be significantly faster. The algorithms can also be easily implemented on a parallel machine of a computer cluster using a system such as MPI in order to solve bigger problems.

4.3 The FFT-based transformation

Let $\psi \in L^2(\mathbf{R}^2)$ a smooth function satisfying a 2D variant of the *admissibility* condition, the three-dimensional continuous beamlet transform of a function $f \in L^2(\mathbf{R}^3)$is given by:

$$\mathcal{B}_f : \mathbf{R}^5 \to \mathbf{R}$$
$$\mathcal{B}_f(a, b_1, b_2, \theta_1, \theta_2) = \int \overline{\psi}_{a,b,\theta_1,\theta_2}(\mathbf{x}) f(\mathbf{x}) d\mathbf{x}.$$

where $a > 0$, $b_1, b_2 \in \mathbf{R}$,$\theta_1 \in [0, 2\pi[$ and $\theta_2 \in [0, \pi[$.

The *beamlet* function is defined by:

$$\psi_{a,b_1,b_2,\theta_1,\theta_2} : \mathbf{R}^3 \to \mathbf{R}$$
$$\psi_{a,b_1,b_2,\theta_1,\theta_2}(x_1, x_2, x_3) = a^{-1/2} \cdot \psi(\quad (-x_1 \sin\theta_1 + x_2 \cos\theta_1 + b_1)/a,$$
$$(x_1 \cos\theta_1 \cos\theta_2 + x_2 \sin\theta_1 \cos\theta_2 - x_3 \sin\theta_2 + b_2)/a);$$

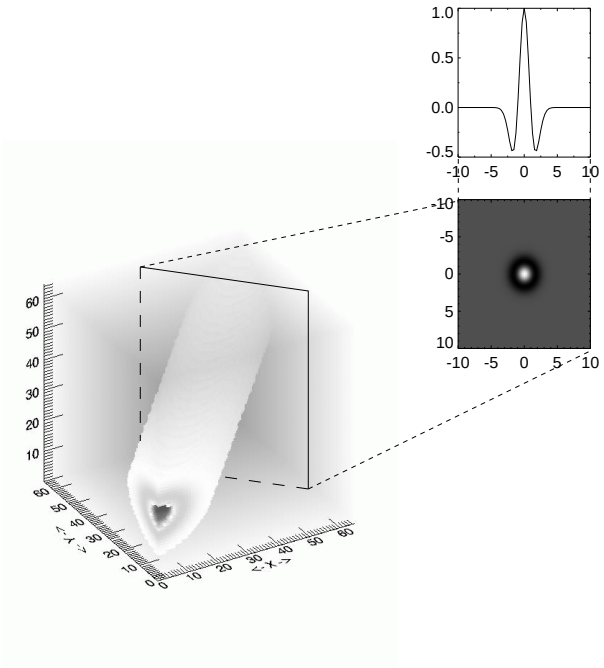

Figure 8: Example of beamlet function.

Figure 4 shows an example of beamlet function. It is constant along lines of direction (θ_1, θ_2), and a 2D wavelet function along plane orthogonal to this direction.

The 3D beamlet transform can be built using the "Generalized projection-slice theorem" [32]. Let $f(\mathbf{x})$ be a function on $\mathbf{R}^n$; and let $\mathcal{R}ad_m f$ denote the m-dimensional partial Radon transform along the first m directions, $m < n$. $\mathcal{R}ad_m f$ is a function of $(p, \mu_m; x_{m+1}, ..., x_n)$, $\boldsymbol{\mu}_m$ a unit directional vector in $\mathbf{R}^n$ (note that for a given projection angle, the m dimensional partial Radon transform of $f(\mathbf{x})$ has $(n - m)$ untransformated spatial dimensions and a (n-m+1) dimensional projection profile). In addition, let $\{\mathcal{F}f\}(\mathbf{k})$ denote the n-dimensional Fourier transform with $\mathbf{x}$ and $\mathbf{k}$ are conjugate variables.

The Fourier transform of the m dimensional partial radon transform $\mathcal{R}ad_m f$ is related to the Fourier transform of f ($\mathcal{F}f$) by the projection-slice relation

$$\{\mathcal{F}_{n-m+1}\mathcal{R}ad_m f\}(k, k_{m+1}, ..., k_n) = \{\mathcal{F}f\}(k\boldsymbol{\mu}_m, k_{m+1}, ..., k_n) \tag{5}$$

Let $c(i_1, i_2, i_3)$ be a cube of size (N, N, N), the Beamlet algorithm consists in the following steps:

1. *3D-FFT.* Compute $\hat{c}(k_1, k_2, k_3)$, the three-dimensional FFT of the cube $c(i_1, i_2, i_3)$.

2. *Cartesian to Spherical Conversion.* Using an interpolation scheme, substitute the sampled

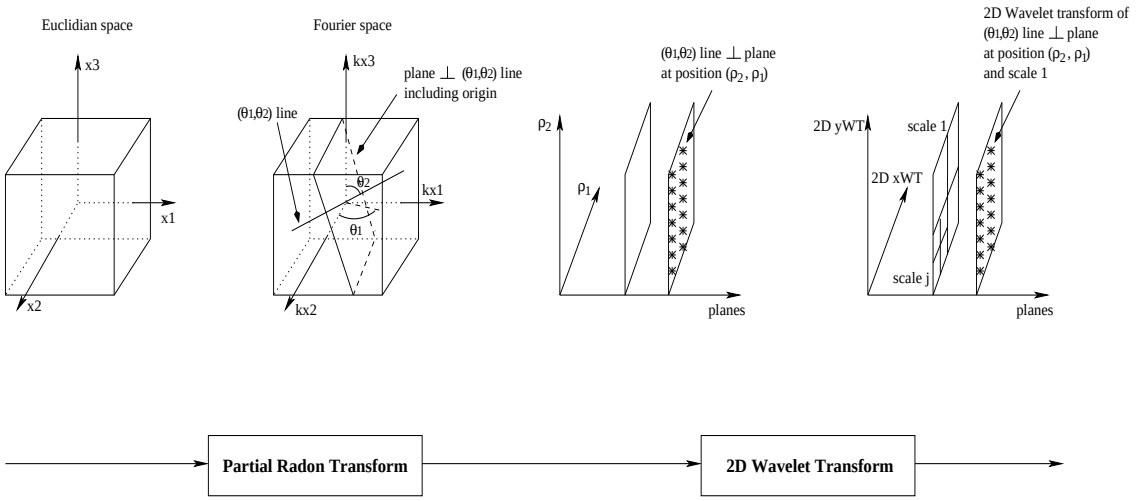

Figure 9: 3D beamlet transform flowgraph.

values of $\hat{c}$ obtained on the Cartesian coordinate system (k_1, k_2, k_3) with sampled values in a spherical coordinate system $(\theta_1, \theta_2, \rho)$.

3. *Extract planes.* Extract the $3N^2$ planes (of size $N \times N$) passing through the origin (each line used in the 3D ridgelet transform defines a set of orthogonal planes; we take the one including the origin).

4. *2D-IFFT.* Compute the two-dimensional inverse FFT on each plane.

5. *2D-WT.* Compute the two-dimensional wavelet transform on each plane.

Figure 9 gives the 3D beamlet transform flowgraph. The 3D beamlet transform allows us to detect filaments in a cube. The beamlet transform algorithm presented in this section differs from the one presented in [7]; see the discussion in [6].

5 Experiments

5.1 Experiment 1

We have simulated three data sets containing respectively a cluster, a plane and a line. To each data set, Poisson noise have been added with eight different background levels. We applied the three transforms on the 24 simulated data sets. The coefficient distribution from each transformation was normalized using twenty realizations of a Poisson noise having the same number of counts as in the data.

Figure 10 shows, from top to bottom, the maximum value of the normalized distribution versus the noise level for our three simulated data set. As expected, wavelets, ridgelets and beamlets are respectively the best for detecting clusters, sheets and lines. A feature can typically be detected with a very high signal-to-noise ratio in a matched transform, while remaining indetectible in some other transforms. For example, the wall is detected at more than 60σ by the ridgelet transform, but less than 5σ by the wavelet transform. The line is detected almost at 10σ by the beamlet transform, and with worse than 3σ detection level by wavelets. These results show the importance of using several transforms for an optimal detection of all features contained in a data set.

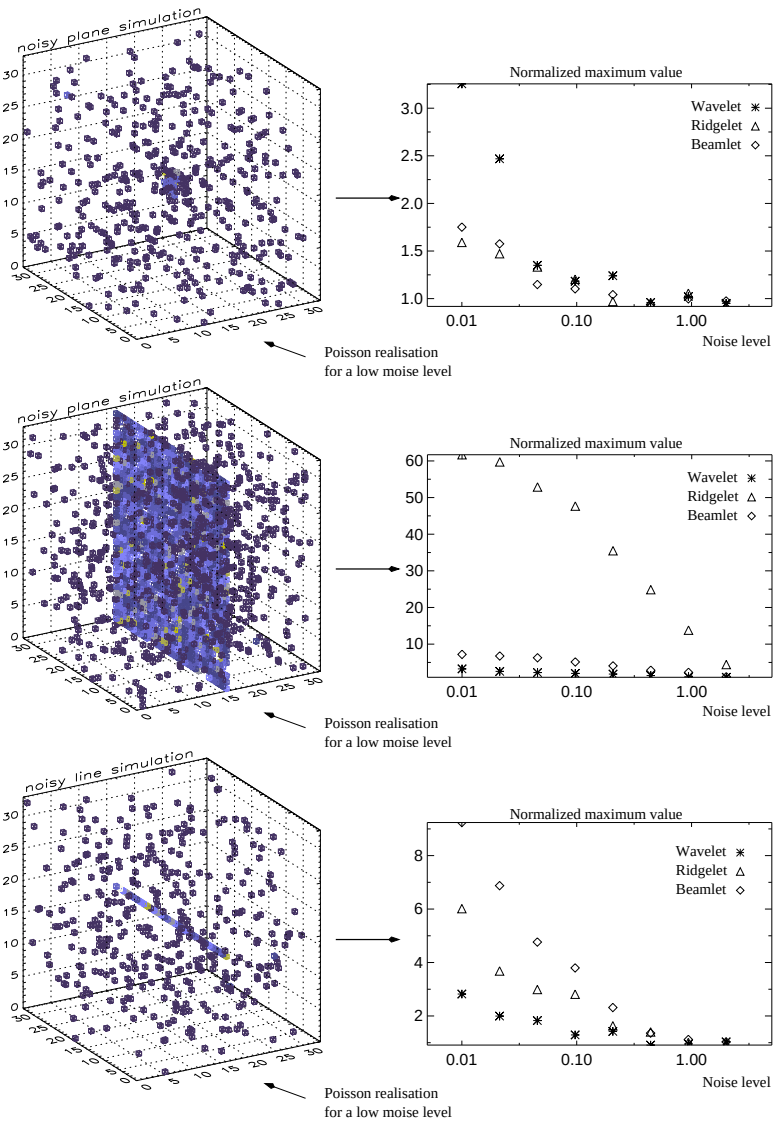

Figure 10: Simulation of cubes containing a cluster (top), a plane (middle) and a line (bottom).

5.2 Experiment 2

We use here two simulated data sets to illustrate the discriminative power of multiscale methods. The first one is a simulation from stochastic geometry. It is based on a Voronoi model. The second one is a mock catalog of the galaxy distribution drawn from a Λ-CDM N-body cosmological model[10]. Both processes have very similar two-point correlation functions at small scales, although they look quite different and have been generated following completely different algorithms.

- The first comes from Voronoi simulation: We locate a point in each of the vertices of a Voronoi tessellation of 1.500 cells defined by 1500 nuclei distributed following a binomial process. There are 10085 vertices lying within a box of 141.4 h^{-1} Mpc side.
- The second point pattern represents the galaxy positions extracted from a cosmological Λ-CDM N-body simulation. The simulation has been carried out by the Virgo consortium and related groups (see `http://www.mpa-garching.mpg.de/Virgo`). The simulation is

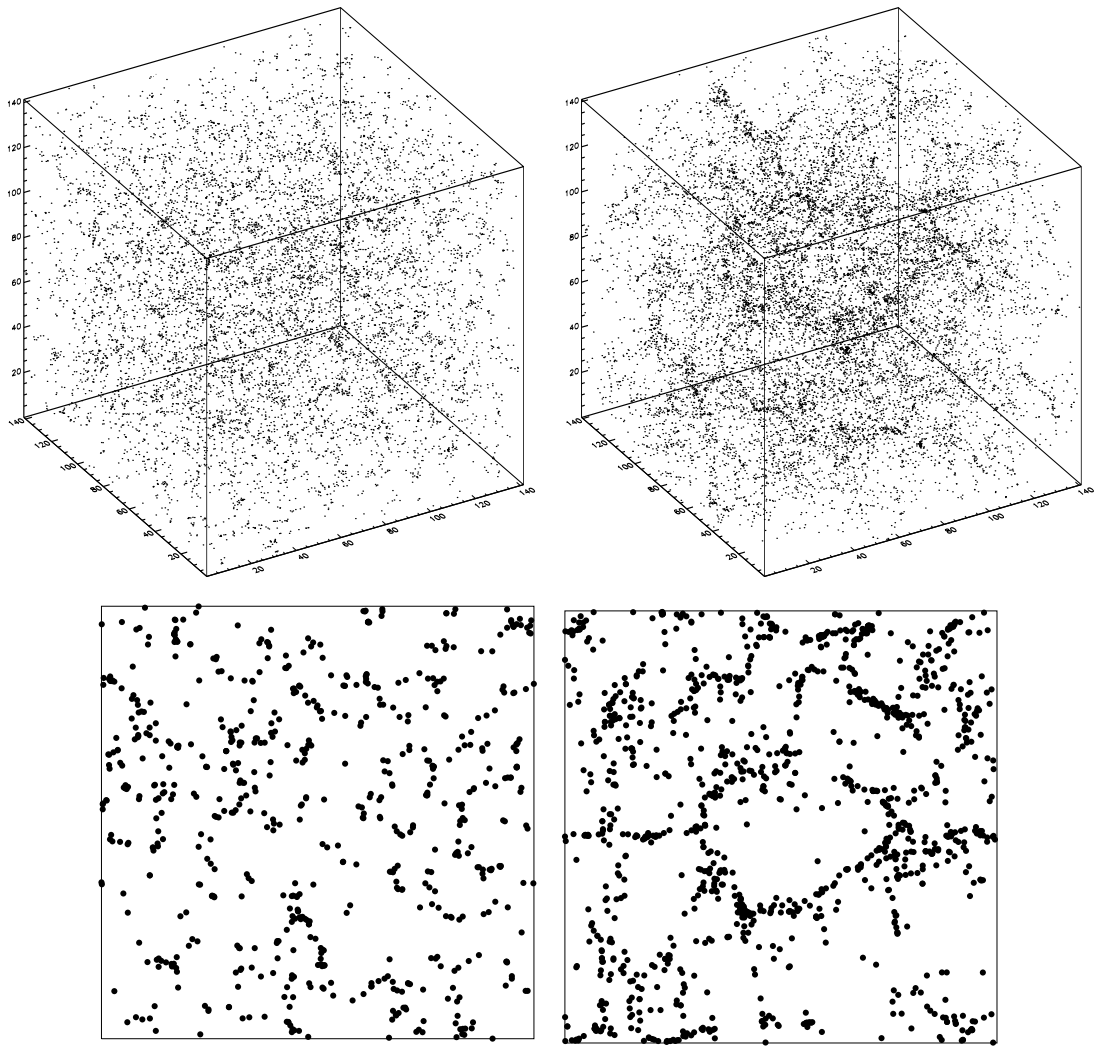

Figure 11: Simulated data sets. Top, the Voronoi vertices point pattern (left) and the galaxies of the GIF Λ-CDM N-body simulation (right). The bottom panels show one 10 h^{-1} width slice of the each data set.

a low-density ($\Omega = 0.3$) model with cosmological constant $\Lambda = 0.7$. It is, therefore, an approximation to the real galaxy distribution[10]. There are 15445 galaxies within a box with side 141.3 h^{-1} Mpc. Galaxies in this catalog have stellar masses exceeding 2×10^{10} $M_{\odot}$.

Figure 11 shows the two simulated data sets, and Figure 12 shows the two-point correlation function curve for the two point processes. The two point fields are different, but as can be seen in Fig. 12, both have very similar two-point correlation functions in a huge range of scales (2 decades).

We have applied the three transforms to each data set, and we have calculated the skewness vector $S = (s_w^j, s_r^j, s_b^j)$ and the kurtosis vector $K = (k_w^j, k_r^j, k_b^j)$ at each scale j. s_w^j, s_r^j, s_b^j are respectively the skewness at scale j of the wavelet coefficients, the ridgelet coefficients and the beamlet coefficients. k_w^j, k_r^j, k_b^j are respectively the kurtosis at scale j of the wavelet coefficients, the ridgelet coefficients and the beamlet coefficients. Figure 13 shows the kurtosis and the skewness vectors of the two data sets at the two first scales. In contrast to the case with the

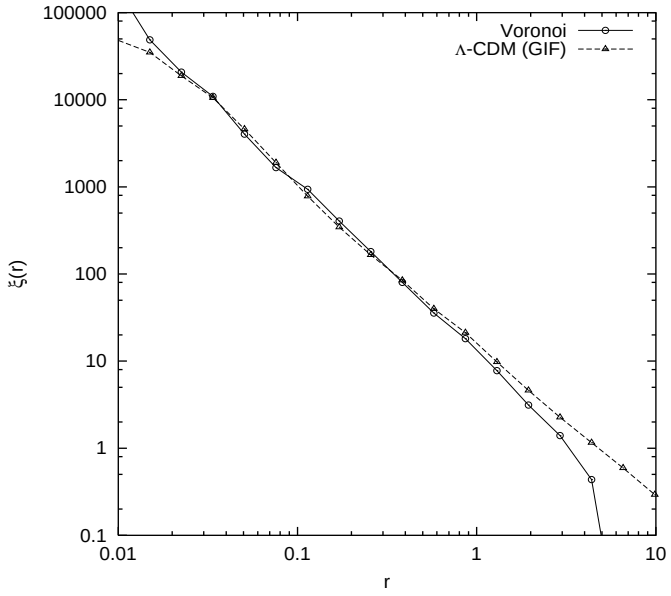

Figure 12: The two-point correlation function of the Voronoi vertices process and the GIF Λ-CDM N-body simulation. They are very similar in the range [0.02,2] h^{-1} Mpc.

two-point correlation function, this figure shows strong differences between the two data sets, particularly on the wavelet axis, which indicates that the second data contains more or higher density clusters than the first one.

5.3 Experiment 3

In this experiment, we have used a Λ-CDM simulation based on the N-body hydrodynamical code, RAMSES [31]. The simulation uses an Adaptive Mesh Refinement (AMR) technique, with a tree-based data structure allowing recursive grid refinements on a cell-by-cell basis. The simulated data were obtained using 256^3 particles and 4.1×10^7 cells in the AMR grid, reaching a formal resolution of 8192^3. The box size was set to $100h^{-1}$ Mpc, with the following cosmological parameters:

$$\begin{aligned} \Omega_m = 0.3 \quad \Omega_\lambda = 0.7 \quad \Omega_b = 0.039 \\ h = 0.7 \quad \sigma_8 = 0.92 \end{aligned} \tag{6}$$

We used the results of this simulation at six different redshifts ($z = 5, 3, 2, 1, 0.5, 0$). Fig. 14 shows a projection of the simulated cubes along one axis. We applied the 3D wavelet transform, the 3D beamlet transform and the 3D ridgelet transform on the six data set. Let $\sigma^2_{W,z,j}, \sigma^2_{R,z,j}, \sigma^2_{B,z,j}$ denote the variance of the wavelet, the ridgelet and the beamlet coefficients of the scale j at redshift z.

Figure 15 shows respectively, from top to bottom, the wavelet spectrum $P_w(z,j) = \sigma^2_{W,z,j}$, the beamlet spectrum $P_b(z,j) = \sigma^2_{B,z,j}$ and the ridgelet spectrum $P_r(z,j) = \sigma^2_{R,z,j}$. In order to see the evolution of matter distribution with redshift and scale, we calculate the ratio $M_{w/b}(j,z) = \frac{P_w(z,j)}{P_b(z,j)}$ and $M_{w/r}(j,z) = \frac{P_w(z,j)}{P_r(z,j)}$.

Figure 16 shows the $M_{w/b}$ and $M_{w/r}$ curves as a function of z and Figure 17 shows the $M^{-1}_{w/b}$ and $M^{-1}_{w/r}$ curves as a function of the scale number j.

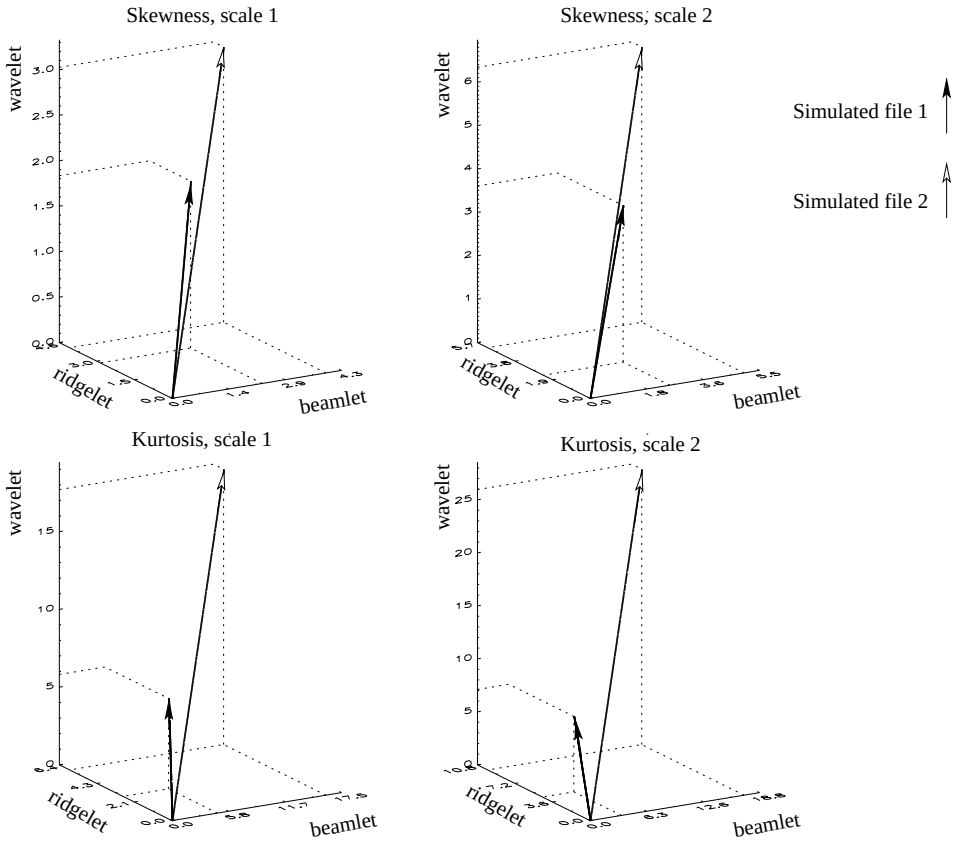

Figure 13: Skewness and kurtosis for the two simulated data set.

The $M_{w/b}$ curve does not show much evolution, while the $M_{w/r}$ curve presents a significant slope. This shows that the beamlet transform is more sensitive clustering than the ridgelet transform. This is not surprising since the support of beamlets is much smaller than the support of ridgelets. $M_{w/r}$ increases with z, reflecting the cluster formation. The combination of multiscale transformations gices clear information about the degree of clustering, filamentarity, and sheetedness.

6 Conclusion

We have introduced in this paper a new method to analyze catalogs of galaxies based on the distribution of coefficients obtained by several geometric multiscale transforms.

We have introduced two new multiscale decompositions, the 3D ridgelet transform and the 3D beamlet transform, matched to sheetlike and filament features respectively. We described fast implementations using FFTs. We showed that combining the information related to wavelet, ridgelet and beamlet coefficients leads to a new description of point catalogs. In this paper, we described transform coefficients using skewness and kurtosis, but other recent statistic estimator such the Higher Criticism [5] could be used as well. Each multiscale transform is very sensitive to one kind of feature: wavelets to clusters; beamlets to filaments; and ridgelets to walls. A similar method has been proposed for analyzing CMB maps [25] where both the curvelet and the wavelet transform were used for the detection and the discrimination of non Gaussianities. This combined multiscale statistic is very powerful and we have shown that two data sets with identical two point correlation functions are clearly distinguished by our approach. These new

tools lead better constraints on cosmological models.

Acknowledgments

We wish to thank Romain Teyssier for giving us the Λ-CDM simulated data used in the third experiment. This work has been supported by the Spanish MCyT project AYA2003-08739-C02-01 (including FEDER), by the Generalitat Valenciana project GRUPOS03/170, and by the National Science Foundation grant DMS-01-40587 (FRG), and by the Estonian Science Foundation grant 4695.

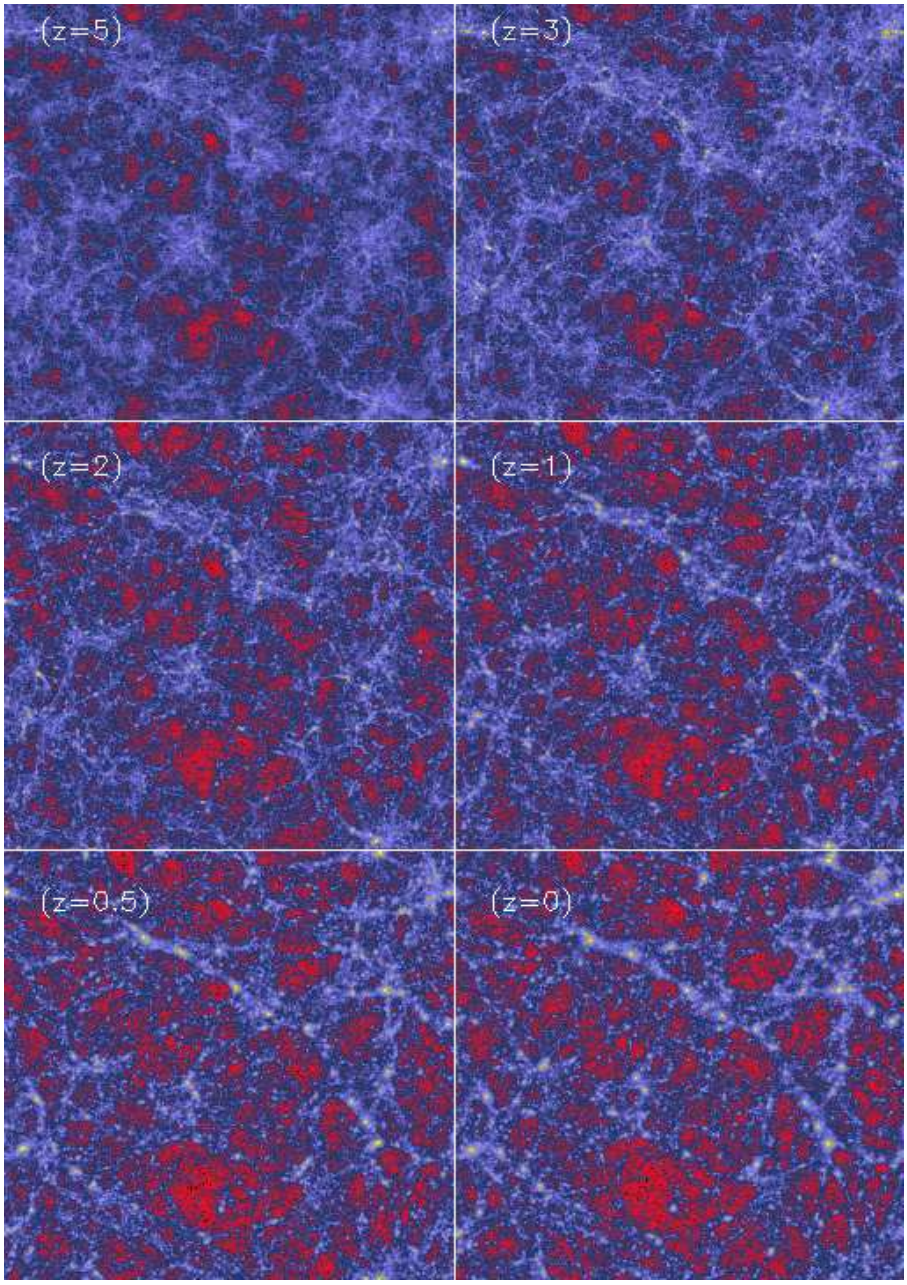

Figure 14: Λ-CDM simulation at different redshifts.

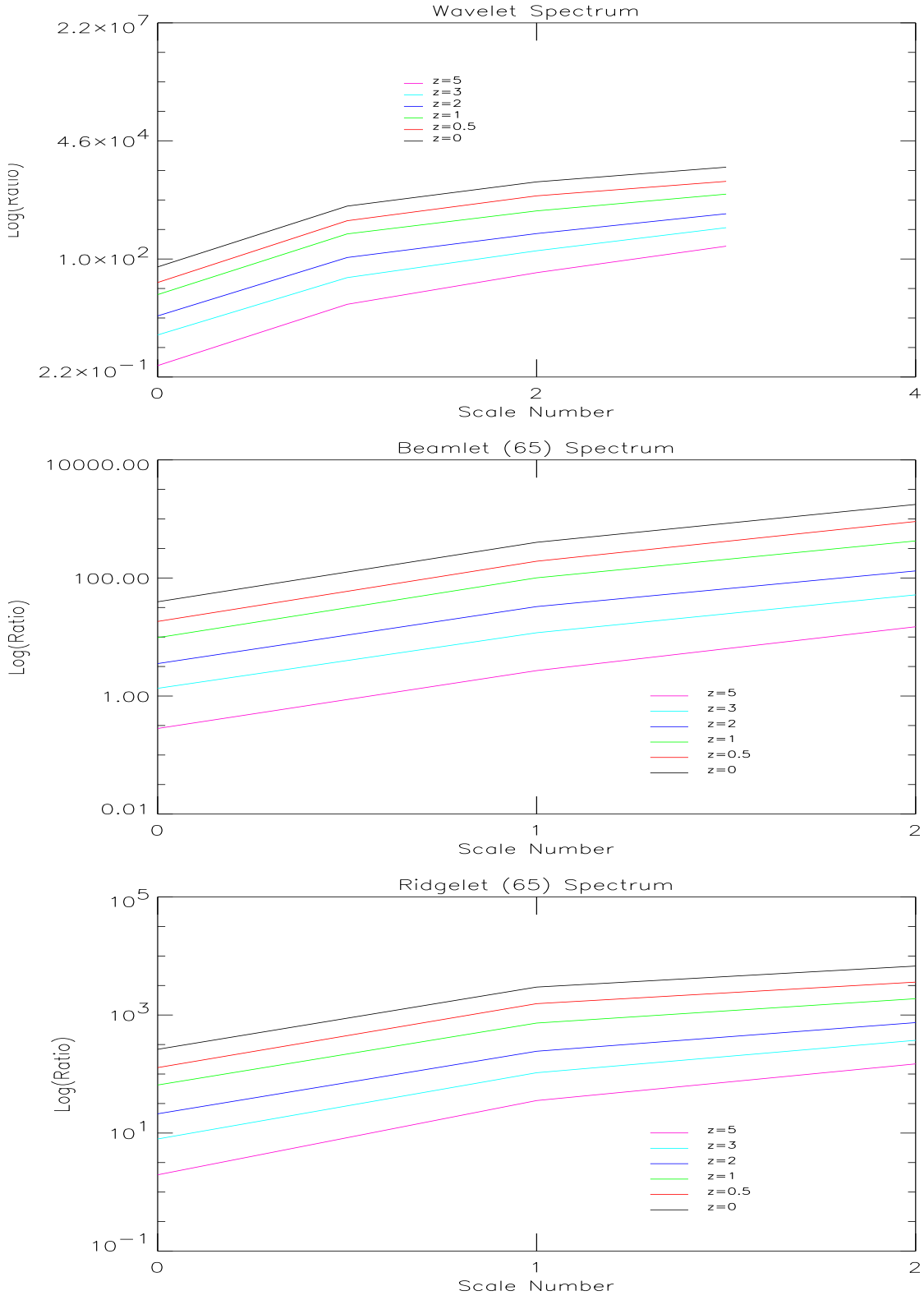

Figure 15: Top, Wavelet spectrum, middle, Beamlet spectrum, and bottom, ridgelet spectrum at different redshifts.

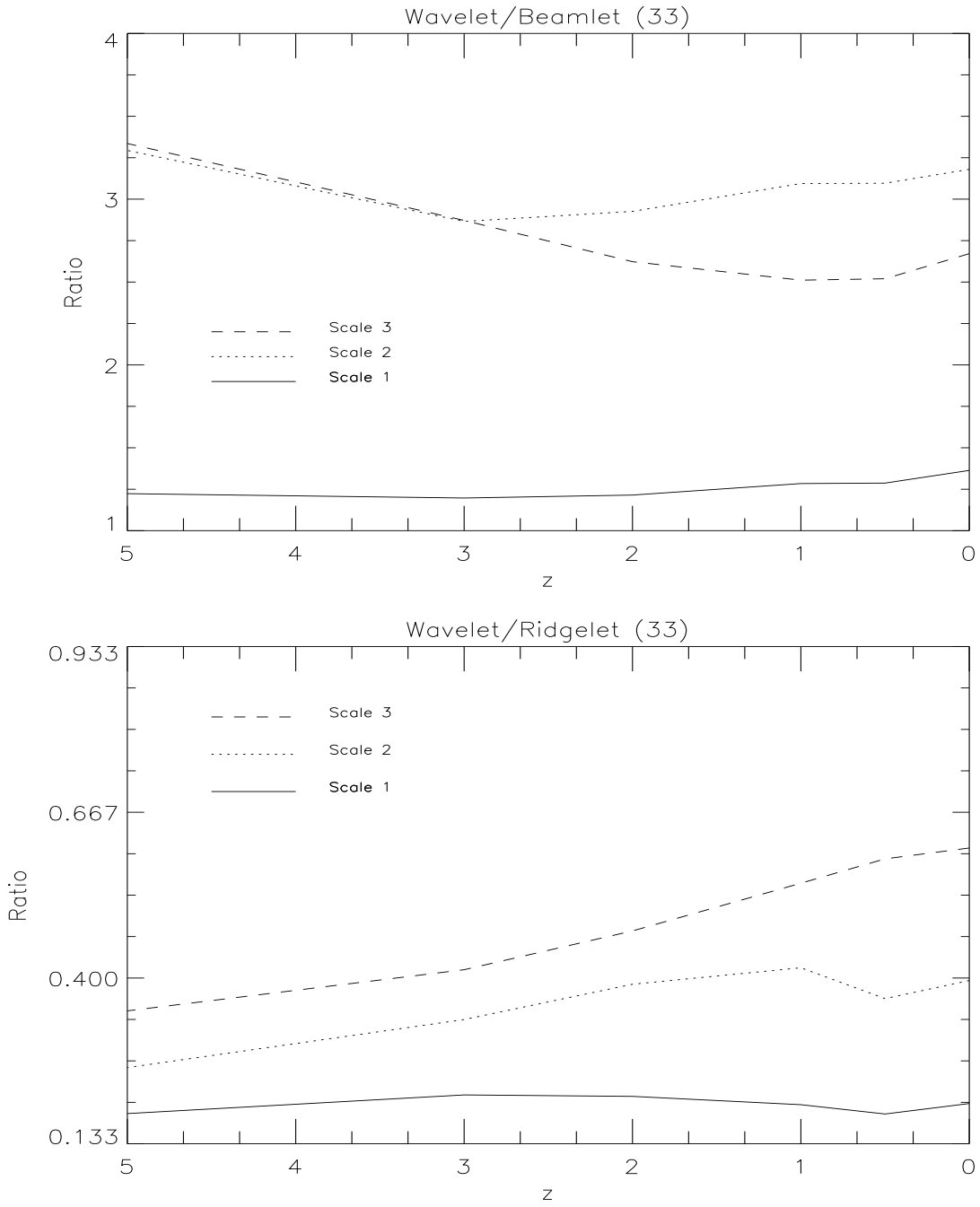

Figure 16: $M_{w/b}(z, j)$ (top) and $M_{w/r}(z, j)$ (bottom) for the scale number j equals to 1,2 and 3.

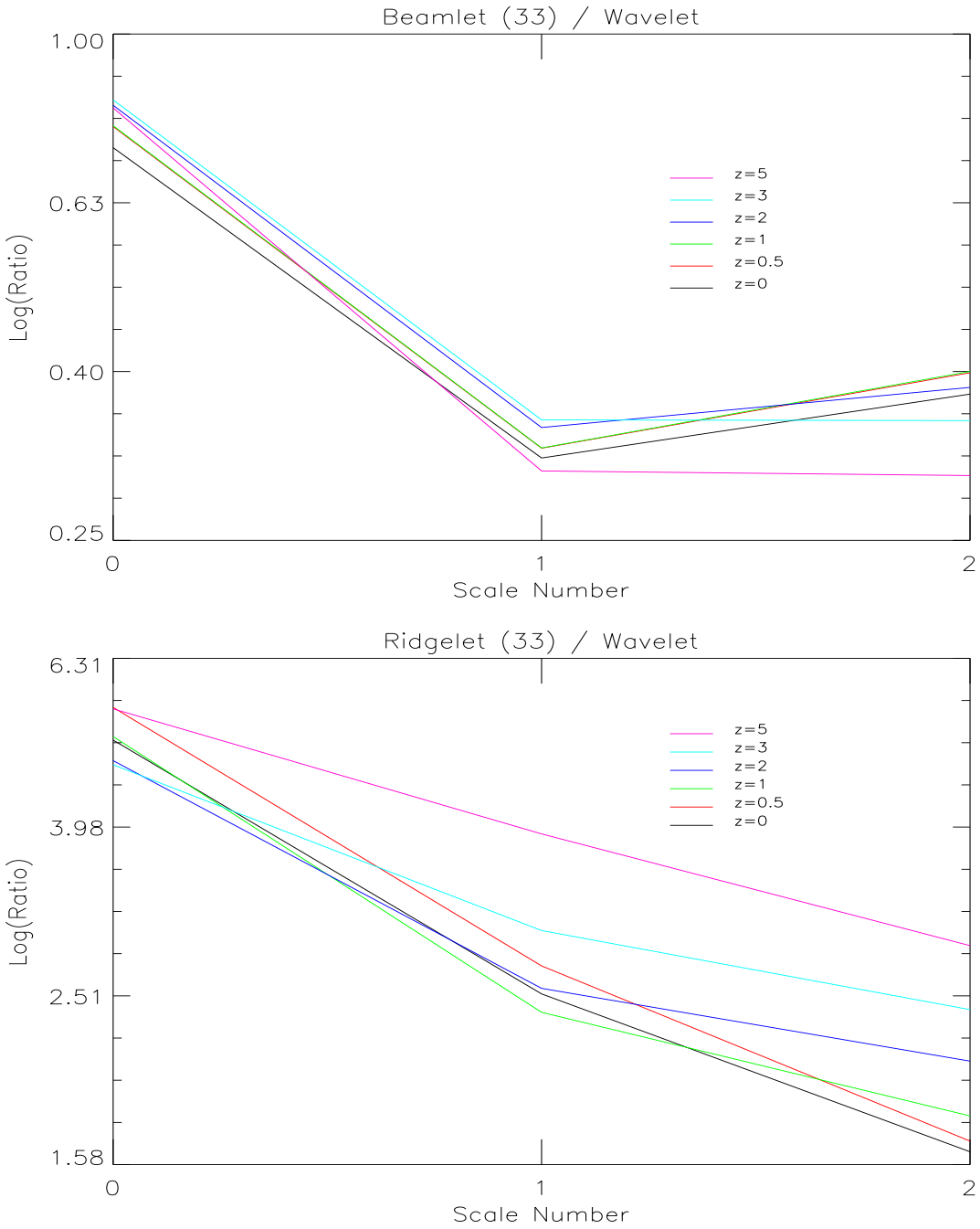

Figure 17: $1/M_{w/b}(z,j)$ (left) and $1/M_{w/r}(z,j)$ (right) at different redshifts.

References

[1] S. P. Bhavsar and R. J. Splinter. The superiority of the minimal spanning tree in percolation analyses of cosmological data sets. *Monthly Notices of the Royal Astronomical Society*, 282:1461–1466, October 1996.

[2] E. J. Candès. Harmonic analysis of neural netwoks. *Applied and Computational Harmonic Analysis*, 6:197–218, 1999.

[3] E.J. Candès and D. Donoho. Ridgelets: the key to high dimensional intermittency? *Philosophical Transactions of the Royal Society of London A*, 357:2495–2509, 1999.

[4] D. Donoho and X. Huo. *Lecture Notes in Computational Science and Engineering*, chapter Beamlets and Multiscale Image Analysis. Springer, 2001.

[5] D. Donoho and J. Jin. Higher criticism for detecting sparse heterogeneous mixtures. *Technical Report , Statistics Department, Stanford University*, 2002.

[6] D.L. Donoho and O. Levi. Fast X-Ray and Beamlet Transforms for Three-Dimensional Data. In D. Rockmore and D. Healy, editors, *Modern Signal Processing*, 2002.

[7] D.L. Donoho, O. Levi, J.-L. Starck, and V.J. Martínez. Multiscale geometric analysis for 3-d catalogues. In J.-L. Starck and F. Murtagh, editors, *SPIE conference on Astronomical Telescopes and Instrumentation: Astronomical Data Analysis II, Waikoloa, Hawaii, 22-28 August*, volume 4847. SPIE, 2002.

[8] A. G. Doroshkevich, D. L. Tucker, R. Fong, V. Turchaninov, and H. Lin. Large-scale galaxy distribution in the Las Campanas Redshift Survey. *Monthly Notices of the Royal Astronomical Society*, 322:369–388, April 2001.

[9] E. Escalera, E. Slezak, and A. Mazure. New evidence for subclustering in the Coma cluster using the wavelet analysis. *Astronomy and Astrophysics*, 264:379–384, October 1992.

[10] G. Kauffmann, J. M. Colberg, A. Diaferio, and S. D. M. White. Clustering of galaxies in a hierarchical universe - I. Methods and results at z=0. *Monthly Notices of the Royal Astronomical Society*, 303:188–206, 1999.

[11] M. Kerscher. Statistical analysis of large-scale structure in the Universe. In K. Mecke and D. Stoyan, editors, *Statistical Physics and Spatial Satistics: The Art of Analyzing and Modeling Spatial Structures and Pattern Formation*. Lecture Notes in Physics 554, 2000.

[12] M. Kerscher, M.J. Pons-Bordería, J. Schmalzing, R. Trasarti-Battistoni, T. Buchert, V.J. Martínez, and R. Valdarnini. A global descriptor of spatial pattern interaction in the galaxy distribution. *Astrophysical Journal*, 513:543–548, 1999.

[13] L. G. Krzewina and W. C. Saslaw. Minimal spanning tree statistics for the analysis of large-scale structure. *Monthly Notices of the Royal Astronomical Society*, 278:869–876, February 1996.

[14] T. Kurokawa, M. Morikawa, and H. Mouri. Scaling analysis of galaxy distribution in the Las Campanas Redshift Survey data. *Astronomy and Astrophysics*, 370:358–364, May 2001.

[15] M.N.M. Van Lieshout and A.J. Baddeley. A non parametric measure of spatial interaction in point patterns. *Statistica Neerlandica*, 50:344–361, 1996.

[16] V. J. Martínez, B. J. T. Jones, R. Domínguez-Tenreiro, and R. van de Weygaert. Clustering paradigms and multifractal measures. *Astrophysical Journal*, 357:50–61, 1990.

[17] V. J. Martínez, S. Paredes, and E. Saar. Wavelet analysis of the multifractal character of the galaxy distribution. *Monthly Notices of the Royal Astronomical Society*, 260:365–375, 1993.

[18] V. J. Martínez and E. Saar. *Statistics of the Galaxy Distribution*. Chapman and Hall/CRC press, Boca Raton, 2002.

[19] S. Maurogordato and M. Lachieze-Rey. Void probabilities in the galaxy distribution — scaling and luminosity segregation. *Astrophysical Journal*, 320:13–25, 1987.

[20] K. R. Mecke, T. Buchert, and H. Wagner. Robust morphological measures for large-scale structure in the Universe. *Astronomy and Astrophysics*, 288:697–704, August 1994.

[21] A. Pagliaro, V. Antonuccio-Delogu, U. Becciani, and M. Gambera. Substructure recovery by three-dimensional discrete wavelet transforms. *Monthly Notices of the Royal Astronomical Society*, 310:835–841, December 1999.

[22] P.J.E. Peebles. *The Large-Scale Structure of the Universe*. Princeton University Press, 1980.

[23] P.J.E. Peebles. The galaxy and mass N-point correlation functions: a blast from the past. In V.J. Martínez, V. Trimble, and M.J. Pons-Bordería, editors, *Historical Development of Modern Cosmology*, Astronomical Society of the Pacific, 2001. ASP Conference Series.

[24] E. Slezak, V. de Lapparent, and A. Bijaoui. Objective detection of voids and high density structures in the first CfA redshift survey slice. *Astrophysical Journal*, 409:517–529, 1993.

[25] J.-L. Starck, N. Aghanim, and O. Forni. Detecting cosmological non-gaussian signatures by multi-scale methods. *Astronomy and Astrophysics*, 416:9–17, 2004.

[26] J.-L. Starck, E. Candès, and D.L. Donoho. The curvelet transform for image denoising. *IEEE Transactions on Image Processing*, 11(6):131–141, 2002.

[27] J.-L. Starck and F. Murtagh. *Astronomical Image and Data Analysis*. Springer-Verlag, 2002.

[28] J.-L. Starck, F. Murtagh, and A. Bijaoui. *Image Processing and Data Analysis: The Multiscale Approach*. Cambridge University Press, 1998.

[29] S. Szapudi and A. S. Szalay. A new class of estimators for the N-point correlations. *Astrophysical Journal Letters*, 494:L41, February 1998.

[30] M. Tegmark, M. R. Blanton, M. A. Strauss, F. Hoyle, D. Schlegel, R. Scoccimarro, M. S. Vogeley, D. H. Weinberg, I. Zehavi, A. Berlind, T. Budavari, A. Connolly, D. J. Eisenstein, D. Finkbeiner, J. A. Frieman, J. E. Gunn, A. J. S. Hamilton, L. Hui, B. Jain, D. Johnston, S. Kent, H. Lin, R. Nakajima, R. C. Nichol, J. P. Ostriker, A. Pope, R. Scranton, U. Seljak, R. K. Sheth, A. Stebbins, A. S. Szalay, I. Szapudi, L. Verde, Y. Xu, J. Annis, N. A. Bahcall, J. Brinkmann, S. Burles, F. J. Castander, I. Csabai, J. Loveday, M. Doi, M. Fukugita, J. R. I. Gott, G. Hennessy, D. W. Hogg, Ž. Ivezić, G. R. Knapp, D. Q. Lamb, B. C. Lee, R. H. Lupton, T. A. McKay, P. Kunszt, J. A. Munn, L. O'Connell, J. Peoples, J. R. Pier, M. Richmond, C. Rockosi, D. P. Schneider, C. Stoughton, D. L. Tucker, D. E. Vanden Berk,

B. Yanny, and D. G. York. The Three-Dimensional Power Spectrum of Galaxies from the Sloan Digital Sky Survey. *Astrophysical Journal*, 606:702–740, May 2004.

[31] R. Teyssier. Cosmological hydrodynamics with adaptive mesh refinement. A new high resolution code called RAMSES. *Astronomy and Astrophysics*, 385:337–364, April 2002.

[32] Paul C. Lauterbur Zhi-Oei Liang. *Principle of Magnetic Resonance Imaging*. IEEE Press, 2000.